Interaction of wavy cylindrical Couette flow with endwalls

Olivier Czarny, Eric Serre, and Patrick Bontoux
LMSNM-GP, UMR 6181, CNRS—Universités d'Aix-Marseille, IMT, La Jetée-Technopôle de Château-Gombert, 38 rue Frédéric Joliot-Curie, 13451 Marseille Cedex 20, France

Richard M. Lueptow[a)]
Department of Mechanical Engineering, Northwestern University, Evanston, Illinois 60208

(Received 24 July 2003; accepted 12 January 2004; published online 8 March 2004)

The finite length of a Taylor–Couette cell introduces endwall effects that interact with the centrifugal instability and the subsequent wavy vortex flow. We investigate the interaction between the endwall Ekman boundary layers and the wavy vortices in a finite-length cavity via direct numerical simulation using a three-dimensional spectral method. To analyze the nature of the interaction between the vortices and the endwall layers, we consider three endwall boundary conditions: fixed endwalls, endwalls rotating with the inner cylinder, and stress-free endwalls. Near the endwalls, the waviness is diminished, primarily due to the effect of the flatness of the endwall rather than as a result of the no-slip boundary condition at the endwall. However, the waviness is present just one or two vortices away from the endwalls, indicating that the effect of the endwall on waviness does not penetrate far from the endwall. The interaction of the waviness with the endwall Ekman layer does not appear to result in disorder in the flow, either in the endwall vortex or farther from the endwall. Likewise, the waviness does not significantly alter Ekman layer thickness from that predicted based on theory. © *2004 American Institute of Physics.* [DOI: 10.1063/1.1652671]

I. INTRODUCTION

Shear flow between a rotating inner cylinder and a fixed outer cylinder, commonly known as Taylor–Couette flow, becomes centrifugally unstable when the rotational speed exceeds a critical value resulting in toroidal Taylor vortices. At higher speeds, a secondary instability results in an azimuthal waviness of the vortices, known as wavy vortex flow. Researchers often consider the flow independent of the confining endwalls: theoretical studies assume that the cylinders are infinitely long; experimental studies use long cylinders compared to the gap between the cylinders; computational studies incorporate periodic boundary conditions to avoid endwall effects. Here we specifically consider the interaction between the boundary-driven flows at the endwalls and the wavy vortices, extending our previous study of the effect of endwalls on the Taylor instability and axisymmetric Taylor vortices.[1]

Far from the endwalls, the radial velocity is zero due to the geostrophic force balance for stable Couette flow. Near the endwalls the no-slip boundary condition upsets the force balance resulting in a radial velocity boundary layer near the endwalls, known as an Ekman layer (although it might be more appropriately considered a Bödewadt flow, since the endwall is usually fixed and the fluid is rotating). The thickness of this boundary layer scales with $(\nu/\Omega)^{1/2}$, where ν is the kinematic viscosity and Ω is an angular velocity scale.[2] This boundary layer flow drives a vortical cell adjacent to the endwall, often called an Ekman vortex.[1,3–5] The Ekman vortex upsets the sharp pitchfork bifurcation for the transition to vortical flow that would occur for infinitely long cylinders resulting in a continuous transition from a featureless stable flow to a cellular flow with the rotation of the vortex adjacent to the endwall defined by the rotation of the Ekman vortex.[1,3–7] Furthermore, the imposition of an endwall prescribes which branch of the bifurcation the flow will prefer—that consistent with the rotation of the endwall Ekman vortex. A flow consistent with a second, disconnected branch corresponding to the vortex adjacent to the endwall rotating opposite that of the Ekman vortex can also occur under certain conditions.[8,9]

It is evident that the endwalls play a significant role in determining the nature of the bifurcation from stable to vortical flow. The endwalls can play an important role for short cylinders even at higher order transitions, since the vortices are never far from the endwalls. For example, the transition from nonwavy Taylor vortices to wavy vortices occurs at a higher rotational speed for short cylinders than for infinitely long cylinders,[10] apparently because the endwall vortices related to the endwall boundary layers impede the transition to wavy vortices. Likewise, the transition from wavy vortex flow to modulated wavy vortex flow occurs at a higher rotational speed for shorter cylinders.[11]

It is the interaction between the endwalls and the wavy vortices that is the topic of this paper. We consider wavy vortex flow between short cylinders for cylindrical Couette flow with the inner cylinder rotating and the outer cylinder fixed, known as the rotor-stator configuration. By using a variety of endwall conditions including fixed endwalls, endwalls rotating with the inner cylinder, and stress-free endwalls (modeling a flat surface without surface tension to

[a)]Author to whom correspondence should be addressed. Telephone: 847-491-4265; fax: 847-491-3915; electronic mail: r-lueptow@northwestern.edu

eliminate the effect of viscosity at the endwall), we investigate the interaction between the endwall boundary layer and the wavy vortical structure.

We used a similar approach to study the transition from nonvortical to vortical flow.[1] In that case, we found that below the critical Taylor number, endwall vortices for rotating endwalls are more than twice the strength of the vortices for fixed endwalls. This trend continues well above the transition to vortical flow, consistent with a simple force balance analysis based on the deviation from geostrophic flow at the endwalls that can be used to determine the magnitude and direction of the endwall boundary layer flow. Stress-free endwalls result in endwall vortices that are similar in strength to those for rotating endwalls above the critical Taylor number. However, fixed endwall and rotating endwall conditions result in vortices that are distorted in the radial direction and axially elongated due to the interaction between the endwall boundary layer and the Taylor vortices. The bifurcation diagram based on the radial velocity near the center of the annulus changes significantly depending on the endwall boundary condition. For stress-free endwall conditions, the bifurcation is quite sharp. Unless the initial conditions are specifically set to favor the other fork of the bifurcation, the fork related to radial outflow at the endwall results when the simulation is started from a zero velocity initial condition. For rotating and fixed endwalls, there is a continuous transition from a featureless flow to a cellular flow because of the development of Ekman vortices well below the critical Reynolds number for the transition from nonvortical to vortical flow.

The case of wavy vortex flow is considerably more complex than that of axisymmetric vortices, primarily because the computations are three-dimensional instead of two-dimensional. In addition, the interpretation of the results is not as clear because the flow is time-dependent. Nevertheless, considering wavy vortex flow in the rotor-stator geometry allows us to further understand the complex interaction between the wavy vortex flow due to the centrifugal instability and the endwall boundary layer flow.

II. GEOMETRY AND NUMERICAL METHOD

The configuration that is considered is an annular cavity between two concentric cylinders of inner and outer radii r_i^* and r_o^*, with the inner cylinder rotating at Ω_i and the outer cylinder fixed. The flow is described by the incompressible, three-dimensional Navier–Stokes equations written using cylindrical coordinates (r^*, z^*, θ) in an absolute frame of reference, according to the velocity–pressure formulation. Parameters characteristic of the physical problem are the Reynolds number $\mathrm{Re}_i = \Omega_i r_i^* d/\nu$, the radius ratio $\eta = r_i^*/r_o^*$, and the aspect ratio $\Gamma = 2h/d$, where $2h$ is the distance between the endwalls, and $d = r_o^* - r_i^*$. The scales for the dimensionless variables of space, time, and velocity are d or h, Ω_i^{-1}, and $\Omega_i r_i^*$, respectively. The dimensionless radial and axial coordinates are $r = (2r^* - r_o^* - r_i^*)/d$, $r \in [-1;1]$, and $z = z^*/h$, $z \in [-1;1]$ to allow the use of Chebyshev polynomials.

On the cylindrical boundaries, the dimensionless velocity (v_r, v_θ, v_z) obeys the no-slip condition

$$v_r = v_z = 0, \quad v_\theta = 1 \quad \text{at } r = -1,\ z \in [-1;1],$$

$$v_r = v_z = 0, \quad v_\theta = 0 \quad \text{at } r = 1,\ z \in [-1;1]. \tag{1}$$

Three endwall conditions are considered, depending on the rotation of the endwall, Ω_e: (1) stationary endwall ($\Omega_e = 0$); (2) rotation of the endwall with the inner cylinder ($\Omega_e = \Omega_i$); and (3) a stress-free boundary condition on the endwall, which is equivalent to a flat, free surface with negligible surface tension (designated $\Omega_e = F$). As described in our previous study of axisymmetric Taylor–Couette flow,[1] the singularity in the azimuthal velocity v_θ at the corner where the cylinder has a different rotational speed than the endwall is handled by forcing the velocity to change exponentially to that of the adjacent cylinder. The dimensionless form of the boundary conditions for the azimuthal velocity at $z = \pm 1$ are

$$v_r = v_z = 0, \quad v_\theta = \frac{e^{-ar} - e^{-a}}{e^a - e^{-a}} \quad \text{for } \Omega_e = 0,$$

$$v_r = v_z = 0, \quad v_\theta = \frac{(1-\eta)r + 1 + \eta}{2\eta} \cdot \frac{e^{-ar} - e^{-a}}{e^a - e^{-a}} \quad \text{for } \Omega_e = \Omega_i, \tag{2}$$

$$v_z = 0, \quad \frac{\partial v_r}{\partial z} = \frac{\partial v_\theta}{\partial z} = 0 \quad \text{for } \Omega_e = F.$$

The region in which the velocity changes from that of the cylinder to that of the endwall is set to about $0.05\,d$, consistent with the gap between the endwall and the cylinder in an equivalent experimental system, by adjusting the decay coefficient a. The distance $0.05\,d$ corresponds to about ten computational mesh points to assure a smooth transition.

The dimensionless incompressible Navier–Stokes momentum equation is

$$\frac{\partial V}{\partial t} + (V \cdot \nabla) V = -\nabla p + \frac{1}{\mathrm{Re}} \Delta V. \tag{3}$$

The solutions to the Navier–Stokes equations are computed using a pseudo-spectral Fourier–Chebyshev collocation method taking advantage of the orthogonality properties of Chebyshev polynomials and providing exponential convergence.[12] The time scheme is semi-implicit and second-order accurate. It is a combination of the second-order backward implicit Euler scheme for the time term, an explicit Adams–Bashforth scheme for the nonlinear terms, and an implicit formula for the viscous diffusion term.[13] The discretized form of the momentum equation is

$$\frac{3V^{j+1} - 4V^j + V^{j-1}}{2\,\delta t} + 2(V^j \cdot \nabla) V^j - (V^{j-1} \cdot \nabla) V^{j-1} = -\nabla p^{j+1} + \frac{1}{\mathrm{Re}} \Delta V^{j+1}, \tag{4}$$

TABLE I. Initial conditions for simulations.

Case	Endwall condition	Initial condition	Perturbation	Final number of vortices	Final waviness
A	$\Omega_e=\Omega_i$	6 axisymmetric rolls	$k_{\text{init}}=3$	6	$k=3$
B	$\Omega_e=\Omega_i$	6 axisymmetric rolls	$k_{\text{init}}=5$	6	$k=2$
C	$\Omega_e=0$	Case B (6 rolls, $k=2$)	⋯	8	$k=2$
D	$\Omega_e=F$	Case C (8 rolls, $k=2$)	⋯	8	$k=2$

where j is the solution at time $t_j=j\,\delta t$, δt being the time step. An improved projection algorithm allows velocity–pressure coupling.[14] The mesh grid is defined by the Gauss–Lobatto collocation points along (r,z) and an equidistant distribution of points in the azimuthal direction, with N, M, and K being the number of radial, axial, and azimuthal points for the spatial mesh. The approximation of flow variables $\Psi=(u,v,w,p)$ is given by

$$\Psi_{NMK}(r,z,\theta,t)=\sum_{n=0}^{N}\sum_{m=0}^{M}\sum_{k=-K/2}^{K/2-1}\hat{\Psi}_{nmk}(t)T_n(r)T_m(z)e^{ik\theta}, \tag{5}$$

where $(r,z,\theta)\in[-1;1]^2\times[0;2\pi]$, T_n and T_m are Chebyshev polynomials, and $\hat{\Psi}_{nmk}$ are the Fourier coefficients. The grid mesh is $N=61$, $M=121$, $K=96$ in the radial, axial, and azimuthal directions, respectively. The high grid resolution in the axial direction is helpful in avoiding any predisposition to a particular number of vortices appearing due to a particular grid spacing. This is the same model that was used in our previous work,[1,15,16] where we have shown that the computational results match those for the transition and shear in the rotor-stator case and are consistent with the expected flow regimes in the counter-rotating cylinders case not accounting for the different aspect ratio and radius ratio. Thus, we are confident that our computational results faithfully reproduce experimental results for geometries similar to those that we study here.

The transition from axisymmetric Taylor vortices to wavy vortices is not firmly established. Experimentally observed points for the transition[17] suggest that for $\eta=0.75$ used in this study $\varepsilon=\text{Re}_i/\text{Re}_{i,\text{crit}}>5$ should result in wavy vortex flow for large aspect ratios Γ, where $\text{Re}_{i,\text{crit}}=85.8$ is the critical Reynolds number for transition to Taylor vortex flow.[18] However, the Taylor instability also depends on the acceleration rate.[19–21] In fact, the flow can revert to nonwavy flow under certain conditions including low aspect ratios.[22] To be sure that the flow would be wavy, the simulations were performed at $\varepsilon=8$. Similar simulations using $\varepsilon=6$ instead of $\varepsilon=8$ resulted in all perturbations being damped within the computational times that were considered and no waviness at all, indicating the difficulty in obtaining wavy vortices for this small aspect ratio. The aspect ratio was $\Gamma=6$.

Different initial conditions were necessary for the computations for the different endwall conditions, as indicated in Table I. For rotating endwalls (cases A and B), the initial condition was that from axisymmetric simulations having six axisymmetric rolls.[1] It was necessary to perturb this axisymmetric flow with a global perturbation of

$$v(r,\theta,z)=0.05\sin(k_{\text{init}}\theta)V(r,\theta,z) \tag{6}$$

in order to generate wavy vortices. Two different azimuthal modes were considered, $k_{\text{init}}=3$ and $k_{\text{init}}=5$. Both resulted in six vortices, but case A retained the initial number of azimuthal modes while case B settled to $k=2$. This multiplicity of solutions for wavy vortex flow is consistent with experiments having much larger aspect ratios[23] and the general nature of Taylor vortex flows. Attempts to simulate a fixed endwall condition (case C, $\Omega_e=0$) using the same method of perturbing the axisymmetric solution were unsuccessful—the azimuthal perturbations were damped, suggesting that the critical conditions may be somewhat dependent on the endwall conditions. Instead, the final solution for case B (six vortices, $k=2$) was used as the initial condition for the fixed endwall condition. The final result maintained two azimuthal waves ($k=2$) but developed eight vortical rolls, presumably due to the splitting of the endwall Ekman vortex into two counter-rotating vortices as a result of the different endwall conditions. (Rotating endwalls result in an outward Ekman layer flow, while fixed endwalls result in an inward Ekman layer flow.) Perturbing an axisymmetric solution with six rolls for stress-free endwalls (case D, $\Omega_e=F$) resulted in the perturbations being damped. Using the final solution for case B (six vortices, $k=2$) as the initial condition also resulted in all perturbations being damped. The only initial condition for which waviness could be obtained was that of the fixed endwall condition (case C, eight vortices, $k=2$). Of course, using previous solutions as the initial conditions for other endwall conditions likely influenced the final flow field, but given the multiplicity of solutions for wavy vortex flow,[23] this is to be expected. Consequently, the results presented here can only be considered as representative of what are likely to be several possible results.

Great care was taken to assure the convergence of the computational solution. The evolution of the nine lowest order modes was tracked over time to be sure that the solution converged to a nontransient result. In all cases, the evolution of the modes clearly showed the transition from one primary azimuthal or axial mode to another having a distinct transient followed by a nontransient, time-dependent final result for a time at least as half as long as the transient.

III. RESULTS

We consider first the general structure of the flow and the vortices for all four cases. A surface at a nondimensional azimuthal velocity of $v_\theta=0.5$, halfway between the azimuthal velocity of the inner cylinder and that of the outer cylinder, is shown in Fig. 1 for each of the cases. The sharp

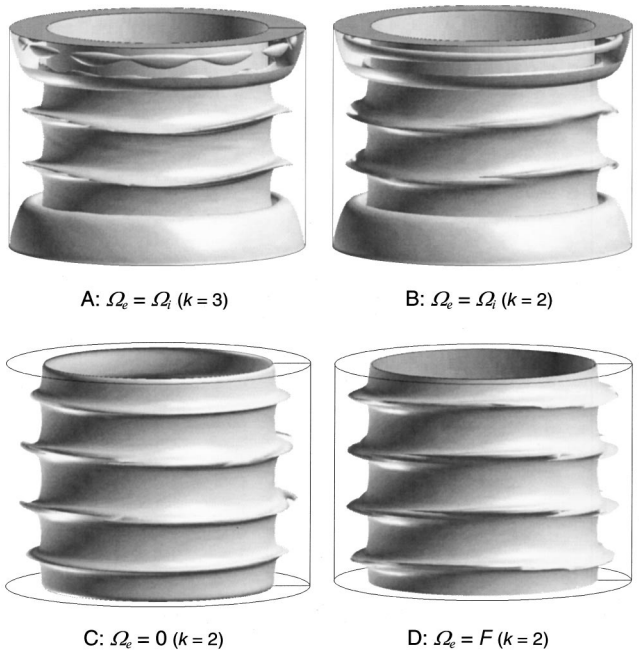

FIG. 1. Visualization of the structure of the flow based on the isosurface corresponding to $v_\theta = 0.5$. For cases A and B, a portion of the isosurface near the top of the annulus is removed to show additional structures. Identical structures are hidden by the isosurface at the lower endwall.

ridges correspond to outflow regions between counter-rotating vortices, where the vortical motion carries high azimuthal momentum fluid from near the inner cylinder toward the outer cylinder. The vortical structures are more readily apparent in Fig. 2, which shows velocity vectors in a meridional plane and, for reference to Fig. 1, the contour corresponding to $v_\theta = 0.5$.

When the endwall is rotating with the inner cylinder in cases A and B ($\Omega_e = \Omega_i$), there are a total of six vortices. The endwall Ekman vortices are substantially elongated to about $1.5\,d$, thereby compressing the Taylor vortices, so that their height is $0.75\,d$ to $0.78\,d$, which is substantially less than the height of $1.002\,d$ expected in the case of infinitely long cylinders.[18] A similar effect was evident for nonwavy vortices, although the endwall vortices were not elongated quite as much. In that case, the length of the endwall vortex increased from $1.17\,d$ to $1.33\,d$ as ε increased from 1.0 to 3.0.[1] Apparently, the endwall vortex continues to lengthen as ε increases to 8.0 in the wavy vortex case studied here. When the endwall is fixed (case C), two extra vortices occur due to the endwall vortex in the initial condition (case B) splitting. This comes about because of the Ekman boundary layer flow at the endwall. For the endwall rotating, the Ekman flow is radially outward at the endwall, but for a fixed endwall, the Ekman flow is radially inward. As a result, when case B for a rotating endwall was used as an initial condition for case C of a fixed endwall, the large endwall vortices evident for case B split into a pair of counter-rotating vortices resulting in a total of eight vortices. Of course, given the aspect ratio, these vortices have a height of about $0.75\,d$. Since case C was used as the initial condition for the stress-free endwall conditions, the same number of vortices with the same rotational sense occurred for the stress-free endwall condition (case D).

In Fig. 1, the waviness is evident in the sharp ridges. The predominant mode, k, of the waviness is more clearly shown in Fig. 3, which is based on contours of radial velocity in a latitudinal plane aligned approximately with the sharp ridges evident in Fig. 1. Mode $k=3$ predominates for case A, while mode $k=2$ is dominant for the other cases. The symmetry of the waves is apparent. This is in sharp contrast to the case of wavy vortex flow with counter-rotating cylinders, where wavy modes are present, but the waves are much more disordered.[24]

The wavy modes are damped near the endwalls as

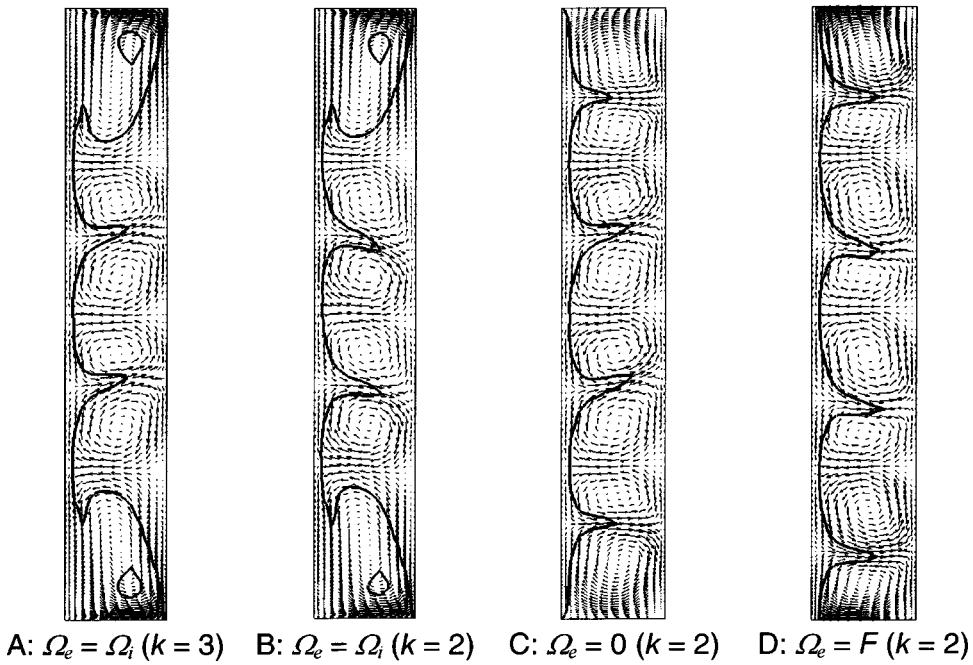

FIG. 2. Velocity vectors in the meridional plane $\theta = 0$ demonstrating the vortical structure of the flow. The single contour on each plot corresponds to $v_\theta = 0.5$. The inner cylinder is the left vertical line; the outer cylinder is the right vertical line.

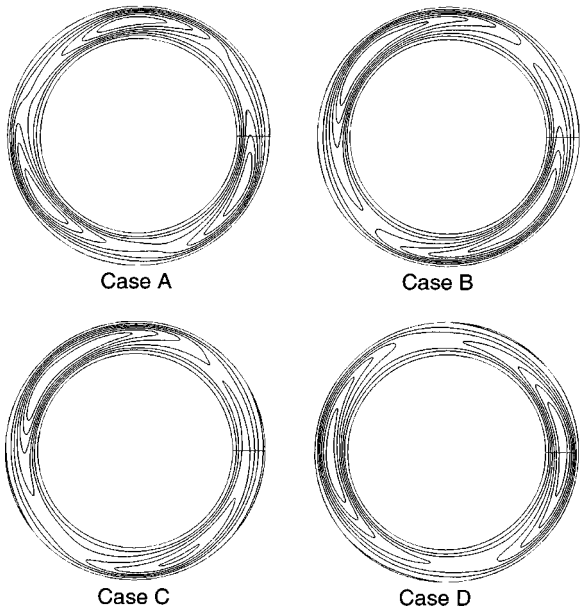

FIG. 3. Contours of v_r showing the azimuthal waviness, where the contours range from 0 to $v_r=0.25$ with $\Delta v_r=0.0357$. Case A: three waves are evident at a position $0.85\,d$ above the mid-plane of the axial length; case B: two waves at $0.85\,d$ above the mid-plane; case C: two waves at $0.62\,d$ above the mid-plane; case D: two waves at $0.62\,d$ above the mid-plane. The horizontal line represents $\theta=0$.

shown in Fig. 4, which depicts radial velocity contours analogous to those in Fig. 3 except in planes within the endwall vortex. (Note that for all cases in Fig. 4 except D, the contour levels are much smaller than in Fig. 3.) When the no-slip condition is imposed on the endwalls, the amplitude of the azimuthal waviness is reduced substantially. In case A, the $k=12$ mode dominates near the endwall over the $k=3$ mode, which is present near the center of the annulus. The $k=12$ mode is also evident at the top of annulus in Fig. 1, where the isosurface is cut away. In case B, the $k=2$ mode is barely evident in the contours, clearly showing how the endwall minimizes the waviness. When the endwall is fixed (case C), the $k=2$ waviness is evident, but greatly diminished from that near the center of the annulus. However, the stress-free endwall (case D) does not reduce the waviness nearly as much, as evidenced by the clear $k=2$ structures shown for this case in Fig. 4.

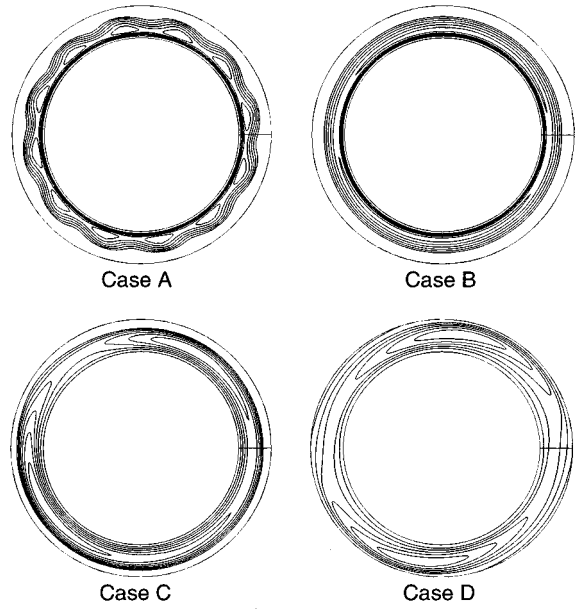

FIG. 4. Contours of v_r showing the azimuthal waviness at $0.57\,d$ from the endwall. Case A: twelve waves are evident; the contours range from 0 to $v_r=0.04$ with $\Delta v_r=0.0057$; case B: two waves of diminished amplitude are barely evident; the contours range from 0 to $v_r=0.04$; case C: two waves of diminished amplitude are barely evident; the contours range from 0 to $v_r=0.04$; case D: Two waves are clearly evident; the contours range from 0 to $v_r=0.25$ with $\Delta v_r=0.0357$.

An important question that arises is if the reduction in the amplitude of the waviness is related to the endwalls being flat or if it is related to the viscous dissipation in the boundary layer at the endwalls. While it may seem obvious that a flat endwall would suppress the axial amplitude of the azimuthal waviness, it is possible that the energy from the axial motion could be transferred to radial or azimuthal motion. Furthermore, it has been shown that the waviness in wavy vortex flow has a substantial radial component.[25] Consequently, a flat endwall alone, in the absence of a viscous boundary layer on the endwall, may not alter the radial wavy motion. In Fig. 4, case D for the stress-free endwall condition indirectly addresses this question. In this case, the amplitude of the waviness near the endwall is present even in the absence of an Ekman layer, although it is somewhat reduced compared to the waviness farther away from the endwall (in Fig. 3). This result is amplified when considering a measure of the total instantaneous spectral energy, E_k, of an azimuthal mode, k, defined as

$$E_k(r,z)=\hat{V}_r^2(k,r,z)+\hat{V}_\theta^2(k,r,z)+\hat{V}_z^2(k,r,z),$$

where $\hat{V}_r(k,r,z)$, $\hat{V}_\theta(k,r,z)$, and $\hat{V}_z(k,r,z)$ are the Fourier coefficients of the respective velocities at meridional position $(r,\,z)$ for azimuthal mode k. Figure 5 shows contour plots of E_k in meridional planes. Two modes are shown for case A, corresponding to the primary azimuthal waviness near the center of the annulus $(k=3)$ and the higher mode waviness $(k=12)$ near the endwall, which is visible in Fig. 1. Only the mode related to the primary azimuthal waviness $(k=2)$ is shown for the other cases. In all situations except case D, the spectral energy for the primary mode is negligible over the entire region occupied by the endwall vortex and most of the next adjacent vortex. Likewise, the spectral energy for modes $k=1$, 3, and 4 (not shown) are negligible in the Ekman vortex for no-slip endwalls (cases A, B, and C). For the higher mode waviness $(k=12)$ that coincides with the Ekman vortex for case A, the mode is present in the Ekman endwall vortex, unlike the low order modes, although it dies out at the endwall.

However, the key case to consider here is that for a stress-free endwall condition (case D), where there is no Ekman layer. In this case, the endwall vortex is driven strictly by the centrifugal instability with no influence of the viscous no-slip boundary condition at the endwall. From Fig. 5, it is clear that there is some energy in the primary mode $k=2$ in

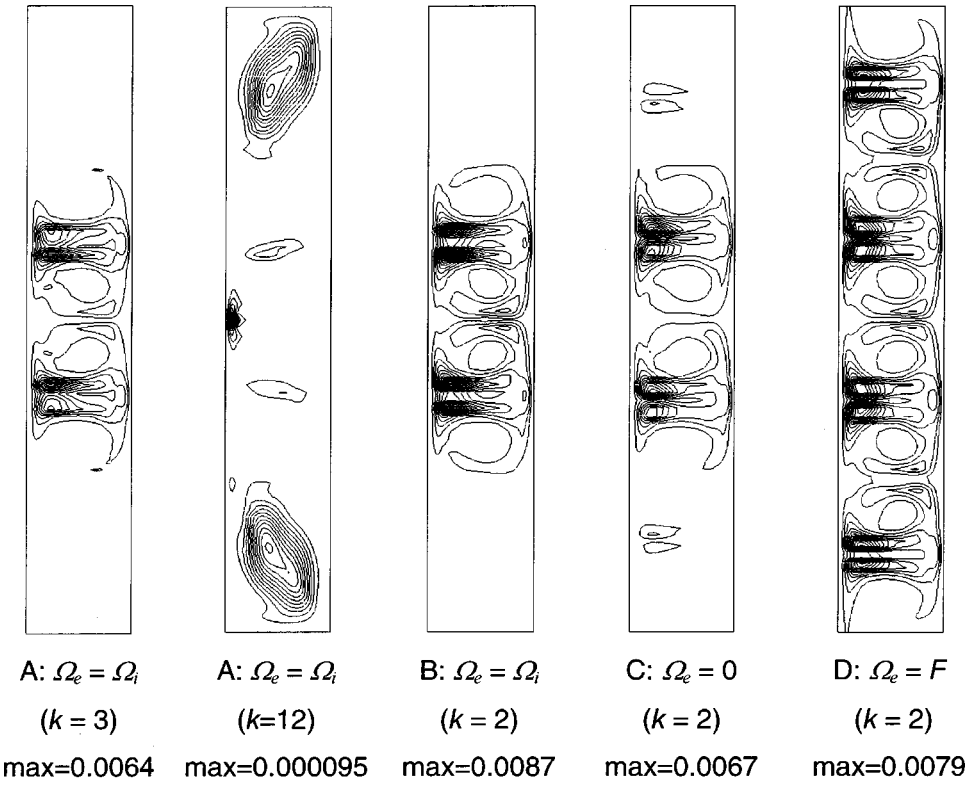

FIG. 5. Contours of a measure of the spectral energy, E_k, for key modes. Contours are equally spaced for all cases from 0 to 0.0088 with $\Delta E_k = 5.87\times10^{-4}$, except case A, $k=12$, where the range is 0 to 9.5×10^{-5} with $\Delta E_k = 6.33\times10^{-6}$. The maximum value for each case is noted. The inner cylinder is the left vertical line; the outer cylinder is the right vertical line.

the endwall vortex. However, the energy is much less on the side of the vortex nearest the endwall than on the other side of the vortex. Furthermore, unlike case C, where there is very little energy in the wavy mode in the vortex adjacent to the endwall vortex, there is substantial energy in this adjacent vortex in case D.

Given that the flat endwall must necessarily suppress axial modes for a stress-free endwall (case D), we would expect that the mode $k=2$ energy at the endwall is primarily in the radial and azimuthal components of velocity. The individual contributions to E_k from the radial, axial, and azimuthal components of velocity are shown in Fig. 6. It is quite clear that the radial and azimuthal contributions to mode $k=2$ are present near the endwall, but are small, while the axial component is zero. In fact, halfway across the gap at the endwall, the radial and azimuthal contributions to the $k=2$ mode are only about 16% of their maximum values that occur along an axial line halfway across the gap. Another way of looking at this is that the radial contribution to the $k=2$ mode is only 6.6% and the azimuthal contribution is only 8.2% of the maximum total energy of the mode that occurs along an axial line halfway across the gap. Of course, for the no-slip endwall conditions, both of these contributions are reduced to zero at the endwall due to the combination of the flat endwall and viscous dissipation. Thus, it is clear that while the flatness of the endwall is most important to the reduced waviness near the endwall, the viscous dissipation in the Ekman layer also plays a small role. At this point it is necessary to note that we carefully checked the evolution of the solution for mode $k=2$ near the endwall to be sure that it achieved a nontransient condition, so it is clear that the flow is fully developed.

Returning to Fig. 5 and comparing it with Fig. 1, it is quite clear that the dominant azimuthal waviness mode is most significant just above and below outflow boundaries, which coincide with the sharp ridges of the isosurfaces of Fig. 1, consistent with experimental results for small Γ.[26] Previous flow visualization results for long cylinders at high Reynolds numbers sometimes indicate that one of the boundaries (either inflow or outflow) is more wavy than the other boundary.[23,27,28] However, it is not possible to determine which boundary is which from the visualization. Measurements of wavy vortices in long cylinders indicate that the inflow boundaries have a larger amplitude of the waves than the outflow boundaries at high Reynolds number.[25] This, of course, contradicts the results presented here that show a greater energy for $k=2$ wavy mode near outflow boundaries. Unfortunately, the contradiction cannot be resolved, other than to say that the multiplicity of solutions that characterizes wavy vortex flow may permit either situation, just as different numbers of waves or vortices can occur.[23]

At this point, we consider the Ekman layer in more detail. Velocity profiles for $v_r(z)$ midway between the inner cylinder and the outer cylinder are shown in Fig. 7 for all three $k=2$ cases. (Although we do not consider the $k=3$ case for a rotating endwall, the results are quite similar to the $k=2$ case for the same endwall conditions.) These profiles are analogous to velocity vector profiles for the axisymmetric case,[1] except that the waviness for the situation considered here requires multiple profiles at different azimuthal positions making it quite difficult to clearly show the profile using velocity vectors. Instead of using vectors in the meridional plane, here we plot the profile of the radial velocity, v_r, in the upper half of the annulus. The contours in Fig. 7 for

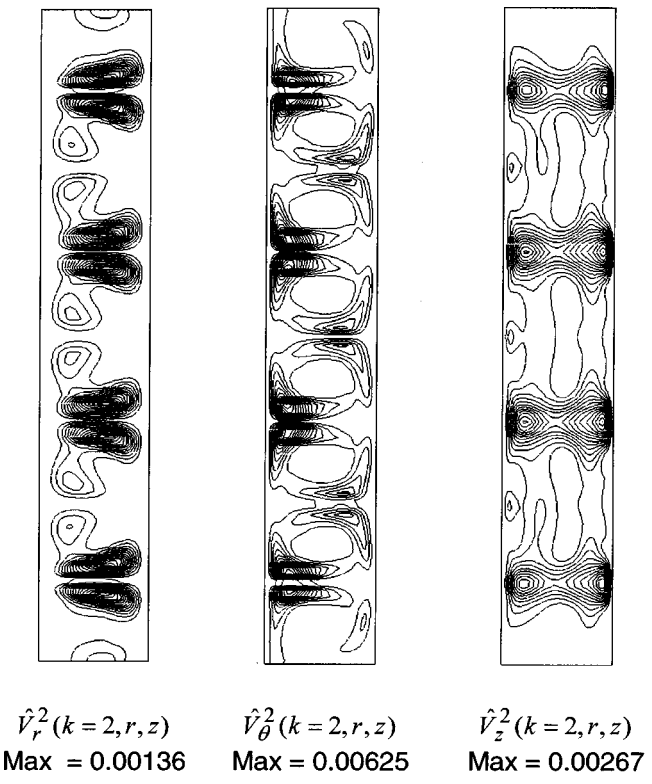

FIG. 6. Contours of $E_{k=2}$ for each velocity component for stress-free endwall conditions. Sixteen contours are equally spaced from 0 to the maximum value. The inner cylinder is the left vertical line; the outer cylinder is the right vertical line.

cases B and C clearly show the Ekman layer near the endwall ($2.9 \leqslant z^*/d \leqslant 3$). Profiles are plotted for several azimuthal positions (as evidenced by the multiple curves in the lower parts of the figure), but very near the endwall the profiles overlay one another for all cases except the stress-free endwall (case D).

The overlapping profiles near the endwall indicate that the Ekman layer thickness remains essentially constant, independent of the waviness of the vortices closer to the center of the annulus. Indeed, measurements of the Ekman layer thickness δ_E based on the axial position of the maximum radial velocity near the endwall show that the thickness does not vary with θ to within the resolution of the calculations. The Ekman layer thickness is related to the Ekman number as $\delta_E/L \sim (Ek)^{1/2} = (\nu/\Omega L^2)^{1/2}$, where L is a length scale in the problem.[2] From the form of the relation, it is clear that the choice of the length scale is not crucial, so we choose to use the gap width d as the length scale. After converting to Re_i and η, the estimated value for the Ekman layer thickness is $\delta_E/d \sim \{\eta/[\mathrm{Re}_i(1-\eta)]\}^{1/2} = 0.066$. This value compares quite well to the Ekman layer thickness indicated in Fig. 7 for case B of $\delta_E = 0.065\,d$, but is substantially less than the Ekman layer thickness of $\delta_E = 0.147\,d$ for case C. Thus, the Ekman layer is a little over twice as thick for the fixed endwalls as for the rotating endwalls (based on the axial position of the maximum radial velocity at the endwall). This result is consistent with the Ekman layer thicknesses for simulations of axisymmetric Taylor vortex flow with differing endwall conditions.[1] In that case, the estimated Ekman layer thickness halfway across the annular gap was $0.19\,d$, and the measured Ekman layer thickness was $0.15\,d$ just above the critical Reynolds number for rotating endwalls (equivalent to case B) and $0.29\,d$ for fixed endwalls (equivalent to case C). Thus, the Ekman layer was just under twice as thick for the fixed endwall as for the rotating endwall. (Note that the Ekman layer thickness was measured slightly differently in the two cases.) The explanation for the difference in thickness for a rotating endwall and a fixed endwall is probably related to the driving force for the Ekman flow. Using a simple prediction scheme for the Ekman boundary layer flow based on the imbalance between the outward centrifugal force and the inward pressure gradient force,[1] one can show that the driving force for the Ekman flow averaged over the endwall is about 3.6 times greater for rotating endwalls than for fixed endwalls. The larger force imbalance drives a faster boundary layer flow for rotating endwalls (as is clear in Fig. 7 for case B), which in turn, results a thinner boundary layer.

Of course, the absence of an Ekman boundary layer for the stress-free boundary condition is quite clear for case D in Fig. 7. Furthermore, the variation in radial velocity that contributes to the mode $k=2$ energy near the endwall (evident in Fig. 6) is quite apparent from Fig. 7 near the endwall.

Several other features are evident in Fig. 7. First, for cases B and C the curves for the velocity profiles at different azimuthal locations overlay one another near the endwall, but spread out moving away from the endwall. Of course, the

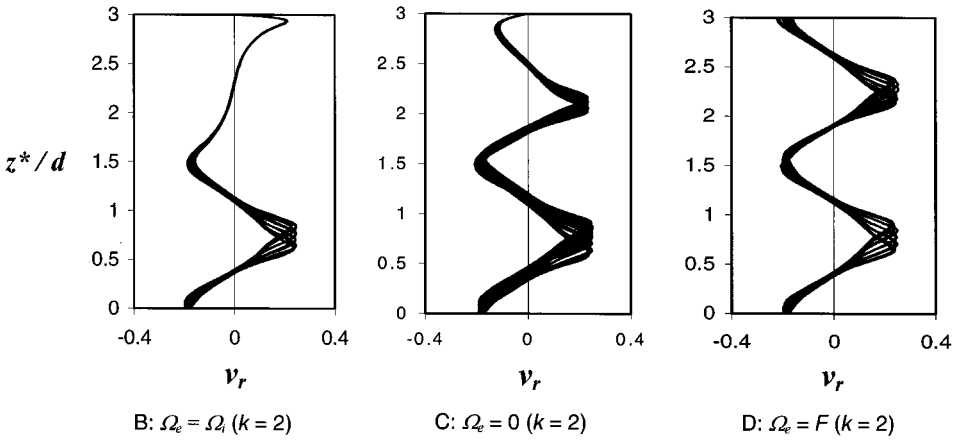

FIG. 7. Radial velocity profiles (v_r) for azimuthal positions $\theta = 0$ to 2π at the center of the gap for the upper half of the annulus. Outward flow is positive.

TABLE II. Waviness as measured by the variation in the axial position of $v_r=0$ (center), maximum v_r (outflow boundary), or minimum v_r (inflow boundary).

Condition	B: $\Omega_e=\Omega_i$ $(k=2)$	C: $\Omega e=0$ $(k=2)$	D: $\Omega_e=F$ $(k=2)$
Center of endwall vortex	0.05 d	0.08 d	0.06 d
Boundary between endwall vortex and adjacent vortex	0.06 d	0.14 d	0.26 d
Outflow boundary ($v_r>0$)	0.23 d	0.30 d	0.30 d
Inflow boundary ($v_r<0$)	0.16 d	0.16 d	0.16 d

spread in the axial direction is a result of the waviness of the vortices, which, as was shown earlier, is largely damped out by the endwalls. The motion of the boundary between vortices can be quantified based on the variation in the axial position of the local maximum/minimum of the radial velocity. Likewise, the axial motion of the center of a vortex can be quantified by the variation in the axial position of the local zero in the radial velocity profiles. Results are presented in Table II.

The waviness of the endwall vortex as measured by the motion of the center of the endwall vortex is small in all cases. The waviness of the boundary between the endwall vortex and the next vortex remains relatively small where there are no-slip endwalls, cases B and C. For the free-slip condition, the motion is much larger, reflecting the reduced impact of the stress-free endwall on reducing the waviness. The waviness of the boundaries between vortices is much larger farther from the endwall for outflow boundaries than for inflow boundaries, as noted with regard to Fig. 5.

A final comment regarding the radial velocity profiles in Fig. 7 is that the maximum radial velocity at outflow boundaries is $v_r\sim 0.25$ and at inflow boundaries is $v_r\sim 0.20$ for the conditions simulated here $(\varepsilon=8)$. This radial velocity is somewhat larger than that seen for nonwavy flow where the radial velocity increases linearly from zero just below $\varepsilon=0$ to a maximum radial outflow velocity of $v_r\sim 0.20$ and a maximum radial inflow velocity of $v_r\sim 0.12$ at $\varepsilon=3$.[1] (In Fig. 12 of Ref. 1, the radial velocity is nondimensionalized by $r_i\Omega_{i,\mathrm{crit}}$, where $\Omega_{i,\mathrm{crit}}$ is the rotational speed at transition from nonvortical to vortical flow.) Thus, it is clear that the strength of the vortical motion continues to grow with increasing Reynolds number into the wavy vortex flow regime. This, of course, is consistent with previous experimental results.[25]

IV. CONCLUSIONS

Although much of the previous research on wavy vortex flow in a cylindrical Couette geometry has avoided the problem of endwall conditions on the flow, we have directly addressed the effect of the endwalls on the flow by altering the endwall conditions computationally. The endwall boundary conditions have a profound effect on the flow for the endwall vortices and the vortices immediately adjacent to the endwall vortices. Clearly, the azimuthal waviness, which has its largest amplitude in the axial direction, is suppressed very near the endwalls simply because the endwalls are flat. The key result here is that even for a stress-free endwall condition, where only the flatness of the endwall plays a role without the effect of the no-slip condition at the wall, nearly all of the energy related to the waviness is suppressed, as shown in Fig. 5. The small amount of energy that remains right at the endwall is divided between radial and azimuthal contributions to the primary azimuthal mode (Fig. 6). Thus, a key result is that the suppression of the waviness is primarily related to the flatness of the endwall and only secondarily related to the no-slip boundary condition.

Surprisingly, the side of the endwall vortex opposite the stress-free endwall is largely unaffected by the flatness of the endwall and has substantial energy related to the waviness, as shown in Fig. 5. The situation is quite different for the no-slip endwall conditions, where nearly all of the energy related to the azimuthal waviness is suppressed in not only the endwall vortex, but also in the vortex adjacent to the endwall (Fig. 5). Thus, it appears that the viscous Ekman flow at the endwall suppresses the waviness further away from the endwall than a flat (stress-free) endwall alone. Nevertheless, the waviness is clearly apparent at the boundary between the vortex adjacent to the endwall vortex and the next vortex, as shown for case B in Fig. 7. Thus, the damping effect of the endwall on the waviness does not penetrate far from the endwall, even for the short annulus considered here.

One might expect that the interaction of the no-slip condition at the endwall with the waviness might lead to a disordered, chaotic behavior either near the endwall or in the entire short annulus, or perhaps a symmetry-breaking condition such as anomalous modes.[9] However, this is not the case. The flow remains well-ordered and symmetric with respect to the dominant azimuthal mode both in the endwall vortex and near the center of the length of the cylinders, as shown in Figs. 1, 3, and 4. However, in one case a mode that is a multiple of the primary azimuthal mode appears near the endwall (case A in Figs. 1 and 4), presumably due to the interaction of the azimuthal waviness with the viscous endwall boundary layer. There is evidence of higher order modes near the endwalls in previous flow visualization results for wavy vortex flow. Specifically, Coles classic paper on the multiplicity of solutions for circular Couette flow includes some figures in which a higher order mode is evident very near the endwalls for some (but not all) cases of wavy vortex flow (see Figs. 16, 19, 20, and 21).[23] However, the flow visualization results indicate a much higher multiple of the primary azimuthal mode (estimated from the photos to be 7 to 10) than the multiple of four evident for case A in Fig. 4 of our simulations, so it is not clear if this is the same phenomenon.

Finally, the waviness away from the endwall does not affect the thickness of the Ekman layer on the endwall. In fact, the predicted layer thickness matches that in the simulations fairly well after accounting for the difference in the driving force for the endwall flow. The endwall boundary layer thickness varies negligibly with azimuthal position in spite of the waviness of the vortices a short distance away.

ACKNOWLEDGMENTS

We gratefully acknowledge the financial support of the Société de Secours des Amis des Sciences (Académie des Sciences, Paris) for O.C. Much of this work was performed during visits by R.M.L. to Laboratory MSNM at Université de la Méditerranée, funded by Direction Scientifique Sciences Pour l'Ingénieur of the Center National de la Recherche Scientifique (CNRS). Thanks also to the scientific committee of the CNRS computing center (IDRIS) for supporting this work and to Richard Kotarba for technical assistance.

[1] O. Czarny, E. Serre, P. Bontoux, and R. M. Lueptow, "Interaction between Ekman pumping and the centrifugal instability in Taylor–Couette flow," Phys. Fluids **15**, 467 (2003).
[2] H. P. Greenspan, *The Theory of Rotating Fluids* (Cambridge University Press, London, 1969).
[3] G. Pfister and I. Rehberg, "Space-dependent order parameter in circular Couette flow transitions," Phys. Lett. **83A**, 19 (1981).
[4] G. Ahlers and D. S. Cannell, "Vortex-front propagation in rotating Couette–Taylor flow," Phys. Rev. Lett. **50**, 1583 (1983).
[5] M. Lücke, M. Mihelcic, and K. Wingerath, "Front propagation and pattern formation of Taylor vortices growing into unstable circular Couette flow," Phys. Rev. A **31**, 396 (1985).
[6] T. Alziary de Roquefort and G. Grillaud, "Computation of Taylor vortex flow by a transient implicit method," Comput. Fluids **6**, 259 (1978).
[7] D.-C. Kuo and K. S. Ball, "Taylor–Couette flow with buoyancy: Onset of spiral flow," Phys. Fluids **9**, 2872 (1997).
[8] T. B. Benjamin, "Bifurcation phenomena in steady flows of a viscous fluid. II. Experiments," Proc. R. Soc. London, Ser. A **359**, 27 (1978).
[9] T. B. Benjamin and T. Mullin, "Anomalous modes in the Taylor experiment," Proc. R. Soc. London, Ser. A **377**, 221 (1981).
[10] J. A. Cole, "Taylor-vortex instability and annulus-length effects," J. Fluid Mech. **75**, 1 (1976).
[11] M. P. Ross and A. K. M. F. Hussain, "Effects of cylinder length on transition to doubly periodic Taylor–Couette flow," Phys. Fluids **30**, 607 (1987).
[12] E. Serre, E. Crespo del Arco, and P. Bontoux, "Annular and spiral patterns in flows between rotating and stationary discs," J. Fluid Mech. **434**, 65 (2001).
[13] J. M. Vanel, R. Peyret, and P. Bontoux, in *Numerical Methods for Fluid Dynamics II*, edited by K. W. Morton and M. J. Baines (Clarendon, Oxford, 1986), pp. 463–475.
[14] I. Raspo, S. Hugues, E. Serre, A. Randriamampianina, and P. Bontoux, "A spectral projection method for the simulation of complex three-dimensional rotating flows," Comput. Fluids **31**, 745 (2002).
[15] O. Czarny, E. Serre, P. Bontoux, and R. M. Lueptow, "Identification of complex flows in Taylor–Couette counter-rotating cavities," C. R. Acad. Sci., Ser. IIb: Mec., Phys., Chim., Astron. **329**, 727 (2001).
[16] O. Czarny, E. Serre, P. Bontoux, and R. M. Lueptow, "Spiral and wavy vortex flows in short counter-rotating Taylor–Couette cells," Theor. Comput. Fluid Dyn. **16**, 5 (2002).
[17] R. C. DiPrima, P. M. Eagles, and B. S. Ng, "The effect of radius ratio on the stability of Couette flow and Taylor vortex flow," Phys. Fluids **27**, 2403 (1984).
[18] A. Recktenwald, M. Lücke, and H. W. Müller, "Taylor vortex formation in axial through-flow: Linear and weakly nonlinear analysis," Phys. Rev. E **48**, 4444 (1993).
[19] J. E. Burkhalter and E. L. Koschmieder, "Steady supercritical Taylor vortices after sudden starts," Phys. Fluids **17**, 1929 (1974).
[20] K. Park, G. L. Crawford, and R. J. Donnelly, "Determination of transition in Couette flow in finite geometries," Phys. Rev. Lett. **47**, 1448 (1981).
[21] T. T. Lim, Y. T. Chew, and Q. Xiao, "A new flow regime in Taylor–Couette flow," Phys. Fluids **10**, 3233 (1998).
[22] Q. Xiao, T. T. Lim, and Y. T. Chew, "Second Taylor vortex flow: Effects of radius ratio and aspect ratio," Phys. Fluids **14**, 1537 (2002).
[23] D. Coles, "Transition in circular Couette flow," J. Fluid Mech. **21**, 385 (1965).
[24] O. Czarny, E. Serre, P. Bontoux, and R. M. Lueptow, "Ekman vortices and the centrifugal instability in counter-rotating cylindrical Couette flow," Theor. Comp. Fluid Dyn. (to be published).
[25] S. T. Wereley and R. M. Lueptow, "Spatio-temporal character of non-wavy and wavy Taylor–Couette flow," J. Fluid Mech. **364**, 59 (1998).
[26] A. Lorenzen, G. Pfister, and T. Mullin, "End effects on the transition to time-dependent motion in the Taylor experiment," Phys. Fluids **26**, 10 (1983).
[27] K. Kataoka, in *Encyclopedia of Fluid Mechanics*, edited by N. P. Cheremisinoff (Gulf, Houston, 1986), Vol. 1, pp. 237–273.
[28] R. J. Donnelly, "Taylor–Couette flow: The early days," Phys. Today **44** (11), 32 (1991).